High-Resolution Imaging and Identification of Biomolecules using Nano-DESI Coupled to Ion Mobility Spectrometry

Daisy Unsihuay,[1] Ruichuan Yin,[1] Daniela Mesa Sanchez,[1] Manxi Yang[1], Yingju Li,[2] Xiaofei Sun,[2] Sudhansu K. Dey,[2] Julia Laskin[1*]

1. *Department of Chemistry, Purdue University, West Lafayette, IN 47907, USA*
2. *Division of Reproductive Sciences, Cincinnati Children's Hospital Medical Centre and Department of Pediatrics, University of Cincinnati College of Medicine, Cincinnati, OH, 45229, USA*

Corresponding author: Julia Laskin, Tel: 765-494-5464, Email: jlaskin@purdue.edu

ABSTRACT

Simultaneous spatial localization and structural characterization of molecules in complex biological samples currently represents an analytical challenge for mass spectrometry imaging (MSI) techniques. In this study, we describe a novel experimental platform, which substantially expands the capabilities and enhances the depth of chemical information obtained in high spatial resolution MSI experiments performed using nanospray desorption electrospray ionization (nano-DESI). Specifically, we designed and constructed a portable nano-DESI MSI platform and coupled it with a drift tube ion mobility spectrometer-mass spectrometer. We demonstrate imaging of drift time-separated ions with a high spatial resolution of better than ~25 μm using uterine tissues on day 4 of pregnancy in mice. Collision cross-section measurements provide unique molecular descriptors of molecules observed in nano-DESI-IM-MSI necessary for their unambiguous identification by comparison with databases. Meanwhile, isomer-specific imaging reveals variations in the isomeric composition across the tissue. Furthermore, ion mobility separation efficiently eliminates isobaric and isomeric interferences originating from solvent peaks, overlapping isotopic peaks of endogenous molecules extracted from the tissue, and products of in-source fragmentation, which is critical to obtaining accurate concentration gradients in the sample using MSI. The structural information provided by the IM separation substantially expands the molecular specificity of high-resolution MSI necessary for unraveling the complexity of biological systems.

INTRODUCTION

Mass spectrometry imaging (MSI) is ideally suited for the simultaneous mapping of the spatial distributions of hundreds of molecules directly from tissues in a label-free fashion [1–6]. MSI is widely used in biomedical research and drug discovery to obtain a better understanding of the molecular-level response of biological systems to different conditions. A majority of MSI applications are focused on the identification of biomarkers and monitoring disease progression [7–9], understanding molecular alterations associated with organ development [10,11], visualizing drug distributions in tissues to identify the mechanisms of their action [12,13], and mapping the biological activity of enzymes by detecting their catalytic products [14]. Desorption electrospray ionization (DESI) [15] and matrix-assisted laser desorption ionization (MALDI) [16–18] are the two most common soft ionization techniques used in MSI. Ambient ionization techniques such as DESI have been employed in MSI experiments to eliminate sample pre-treatment prior to analysis and enable imaging of biological samples in their native state. Nanospray desorption electrospray ionization (nano-DESI) developed by our group [19] is an ambient liquid extraction-based ionization technique, which has been used for imaging of biological tissues with high sensitivity and high spatial resolution of ~10 μm [20]. Furthermore, we and others have demonstrated the quantitative capabilities of nano-DESI MSI and its ability to measure accurate concentration gradients in biological samples by normalizing the signals of endogenous molecules to the signals of internal standards added to the extraction solvent [21–23].

In the past two decades, substantial efforts have been dedicated to improving the spatial resolution, data processing, and speed of analysis of MSI [5]. However, on-the-fly identification of molecules in MSI experiments is challenging. Furthermore, the presence of some isobaric and isomeric species, which cannot be separated by *m/z* alone complicates the interpretation of MSI data necessary for the molecular-level description of complex biological systems. Some of these challenges have been addressed using tandem mass spectrometry (MS/MS) imaging experiments, which enable simultaneous imaging and identification of molecules in biological samples [24,25]. In addition, derivatization approaches including online singlet oxygen reaction [26] and on-tissue Paternò−Büchi [27] or ozonolysis reactions [28] have been coupled with MSI for studying the localization of positional isomers of phospholipids. However, these experiments are typically limited to a targeted list of *m/z* windows. Therefore, coupling MSI with structurally sensitive techniques is a promising approach for the untargeted analysis with improved coverage and structural characterization of molecules in biological samples.

Ion mobility spectrometry (IMS) separates molecules based on their size, shape, and charge [29,30] and operates on a millisecond time scale, which facilitates its integration into MSI experiments [31,32]. Furthermore, drift tube ion mobility spectrometry (DTIMS) provides structural information in the form of

collision cross sections (CCS) of the separated ions [33–35]. An interlaboratory study has demonstrated that CCS values are reproducible across different experimental platforms [36], which makes them excellent molecular descriptors and enables confident annotations of numerous biomolecules using open-source databases [37–39].

Several ion mobility instruments have been successfully coupled with MSI techniques including MALDI [40,41], DESI [42,43], liquid extraction surface analysis (LESA) [44], laser desorption electrospray ionization (LAESI) [45], and infrared matrix-assisted laser desorption electrospray ionization (IR-MALDESI) [46]. The advantages of such coupling include improved molecular coverage, the ability to generate background-free images, and rapid isomeric separation [31,47].Herein, we describe for the first time the design and performance of a portable high-resolution nano-DESI MSI platform coupled to a linear ion mobility quadrupole time-of-flight mass spectrometer (IM-QTOF MS), which combines the sensitivity, quantitative capability, and high spatial resolution of nano-DESI MSI with on-the-fly separation of isomeric analytes and their structural characterization using CCS measurements. In comparison with other ion mobility systems, DTIMS provides direct structural information without the need for external calibration, which facilitates the identification of biomolecules observed in nano-DESI MSI experiments. Proof-of-concept IM-MSI experiments using sections of mouse uteri on day 4 of pregnancy prior to embryo implantation demonstrate the capabilities of this newly-developed platform for imaging of drift time-selected biomolecules with a spatial resolution better than 25 μm. We demonstrate that ion mobility (IM) separation relaxes the requirement imposed on the mass resolving power of a mass analyzer by separating isobaric species along the drift time axis, enables separation of isomeric species, facilitates the identification of biomolecules observed in MSI experiments, and eliminates interferences from solvent-related peaks and peaks resulting from gas-phase fragmentation of chemically labile endogenous molecules. In combination with the previously reported quantitative capabilities of nano-DESI MSI [48], this platform opens up new research directions focused on isomer-selected quantitative imaging of complex biological samples. Furthermore, the newly developed versatile platform can be coupled to any mass spectrometer making it broadly applicable to a variety of applications.

EXPERIMENTAL SECTION

Chemicals.

LC-MS grade methanol (MeOH) and LC-MS water were purchased from Sigma-Aldrich (St. Louis, MO).

Tissue Samples.

Uterine tissues on day 4 of pregnancy were retrieved from the C57BL/6 mixed background pregnant mice on day 4 morning as described in our previous studies [25,49]. The mice were housed in the Cincinnati Children's Hospital Medical Center Animal Care Facility according to National Institutes of Health and institutional guidelines for the use of laboratory animals and animal handling protocols of the approved by Cincinnati Children's Hospital Research Foundation Institutional Animal Care and Use Committee. Pieces of mouse uteri on day 4 of pregnancy were snap-frozen and sectioned using a cryostat. Sections of 12 μm thickness were mounted onto glass slides and stored in a -80 ºC freezer prior to analysis.

Instrument description:

Nano-DESI MSI experiments were performed on an Agilent 6560 IM-QTOF MS (Agilent Technologies, Santa Clara, CA). A schematic of the nano-DESI source is shown in Figure 1a. Figures 1b and 1c show the nano-DESI imaging system developed in this study which is assembled on a portable cart (1) that can be readily deployed in combination with any mass spectrometer. The cart houses all the components including a vibrationally insulated platform (2) (Newport, Irvine, CA), a lock-in amplifier (3) (Stanford Research Systems, Sunnyvale, CA) and a computer that controls the system (4). The XYZ stage (5) and sample holder are mounted on the vibrationally insulated platform, along with the micro-positioners (6) and Dino-Lite cameras (7). A stainless steel capillary extension (8) is attached to the mass spectrometer inlet as shown in Figure 1c. The nano-DESI probe is described in the next section. A pulse of 5V to 0V provided by the LabView program is used to synchronize the XYZ stage and Agilent's acquisition software. Typical source parameters are as follows: capillary temperature of 300 ºC, ESI voltage of +4.5 kV for positive mode and -4.0 kV for negative mode.. Manual tuning was carried out to optimize most of the internal voltages and trapping and release times. Briefly, we use a mixture of standards covering the *m/z* range of 100-1500 which is used in our imaging experiments. We optimize the front funnel settings to minimize in-source fragmentation and improve signals at the low and high mass range in both modes. These parameters can be found in Tables S1-S2. We reproduced the drift tube parameters reported previously in the inter-laboratory study [36], which uses the same DTIMS instrument used in this work. The detailed drift-tube settings can be found in Tables S3-S4. Finally, we evaluated the signal response to different trapping and release times and selected the parameters that enabled the best transmission of most of the standards without saturating the detector. A trapping time of 15 ms and a release time of 150 μs were selected for positive mode experiments. Meanwhile, a trapping time of 15 ms and a release time of 300 μs were selected for negative mode experiments.

Nano-DESI MSI:

Imaging experiments of uterine tissue sections were performed in triplicate using a mixture of MeOH:H_2O (9:1) (v/v), which was infused using a syringe pump (KD Scientific, Holliston, MA) at 0.5 μL/min. The high-resolution nano-DESI probe is assembled in front of the mass spectrometer inlet as shown in Figure 1 and described in our previous studies [50,51]. Briefly, the finely pulled primary (9) and nanospray (10) capillaries with OD of 15-25 μm are aligned to form a liquid bridge. Analyte molecules are extracted into the liquid bridge directly from the tissue and transferred to a mass spectrometer inlet through the nanospray capillary. A third capillary (11), that serves as a shear-force probe [51], is positioned in close proximity to the nano-DESI probe to maintain a constant distance between the sample and the nano-DESI probe. Imaging data are acquired in lines by scanning the sample under the nano-DESI probe in one direction and stepping between the lines in another direction. For all the data reported in this study, we used a scan rate of 20 μm/s and a step between the lines of 29 μm resulting in a total analysis time of ~3 h per tissue section (~4 mm^2). Experiments were performed using an acquisition rate of 1 Hz resulting in an average pixel size of 20 × 29 $μm^2$. MS/MS data for most of the endogenous species observed in nano-DESI MSI experiments were acquired directly from tissue sections using the auto MS/MS mode at a collision energy of 20 V.

Data processing

The initial lipid and metabolite annotation is performed based on the accurate mass measurements using LIPID MAPS (www.lipidmaps.org) and METLIN (https://metlin.scripps.edu). Then, the CCS values are calculated for each molecule from the raw drift time values obtained using the single-field method. Next, the initial annotations are verified by comparing the measured CCS values with the values from the CCS compendium [37]. Finally, the assignments are confirmed using the MS/MS data acquiredas described earlier.

Analysis of the QTOF data is performed using the Ion Mobility-Mass Spectrometry Image Creator script developed by our group [52]. In brief, the script interfaces with Skyline's [53] command line to input experimental .d data files and export a chronogram summary of targeted masses. The script then reconstructs those chronograms into individual ion images. The resulting images are displayed using a self-normalized heat map color scale. Intensity values for each pixel are normalized to the TIC. For data with drift time information, Agilent's MassHunter Mass Profiler software is used to extract a feature list, i.e. a list containing *m/z*, drift time, and charge information of recurring peaks among all the experimental lines.

RESULTS AND DISCUSSION

Herein, we describe the implementation of the high-resolution nano-DESI MSI on an Agilent 6560 IM-QTOF system. We demonstrate the capabilities of this new platform in combination with IM separation,

which enables both *m/z*- and ion mobility-selected imaging of molecules in tissues. We use mouse uterine tissue on day 4 of pregnancy as a model system, which is a fairly small sample (< 2 mm in diameter) with distinct anatomical features described later in the text and substantial chemical gradients between the different regions of the tissue [50].

Nano-DESI imaging of drift-time separated ions

Figure 2 shows the averaged mass spectra (top) and CCS vs. *m/z* 2D plots (bottom) of all the species identified in the uterine sections using nano-DESI-IM-MSI experiments in a) positive and b) negative mode. These data were extracted from a line scan corresponding to the central region of the tissue. We observe that phosphatidylcholine (PC) species are abundant in the *m/z* range of 760-880 in positive mode whereas fatty acid (FA) species in the *m/z* range of 250-400 are dominant in negative mode. We successfully detected 227 unique species containing 161 lipids and 66 metabolites. Specifically, 131 species were identified in positive mode, 109 species were identified in negative mode, and 13 species were found in both modes. The distribution of different classes of molecules observed in nano-DESI IM-MSI experiments is shown in Figure S1 and the assignments are summarized in Tables S4-S5. An expanded view of the positive mode CCS vs. *m/z* plot in the *m/z* 760-880 range is shown in Figure 2c. Phospholipids observed in this region of the spectrum, are grouped into distinct homologous series based on their lipid class-specific CCS-mass correlations. For each adduct type and lipid class indicated by different markers and colors in Figure 2c, the homologous series differing by the number of double bonds follow distinct linear trends in CCS as a function of *m/z*. Each of these series is highlighted with a dotted line and labeled using the AA:X notation, in which AA indicates the acyl chain length containing X double bonds. The number of double bonds in each species is indicated inside the corresponding marker in the plot. Structural differences pertaining to the lipid class and type of adduct are readily visualized based on their CCS vs. *m/z* trend lines. For example, it is easy to distinguish different adducts of PC and PE species of varying length of fatty acyl tails. We observe that for the same adduct and length of acyl chains, PE species are characterized by smaller CCS values indicating a better packing efficiency of these molecules in comparison to PC species [54]. Moreover, IM separation highlights structural changes within the same homologous series of species. For example, for the same lipid class, type of adduct, and acyl chain length, the CCS value decreases with an increase in the degree of unsaturation. The addition of a double bond introduces a kink into the acyl chain, which makes the molecule more compact and enables it to travel faster through the drift tube.

Similarly, FAs observed in the negative mode CCS vs. *m/z* plot shown in Figure 2d are grouped based on the length of the acyl chain. Interestingly, oxidized FAs (pink circles in Figure 2d) display different slopes for different groups of species. This observation likely indicates the presence of different classes of

oxidized FAs such as oxo-FAs, hydroperoxides, or epoxides in the tissue sample. Because of the low abundance of these molecules and uninformative fragmentation patterns observed in MS/MS experiments it is difficult to characterize their structures. Nevertheless, their CCS values listed in Table S5-S6 are consistent with their classification as oxidized FAs [37,55] . These observations highlight the power of the CCS measurement for the identification of compounds observed in MSI experiments based on the predictable differences in the trend lines exhibited by every lipid class.

We also took advantage of the measured CCS values to improve the confidence of our metabolite annotations. For example, a feature at *m/z* 346.0553 could be assigned as the $[M-H]^-$ ion of either adenosine monophosphate (AMP) or deoxyguanosine monophosphate (dGMP), which are isomeric. The collected MS/MS spectrum for *m/z* 346.0553 (Figure S2a) is dominated by fragments at *m/z* 78.9596 and 96.9726 corresponding to the loss of the phosphate group. Because both isomers contain phosphate groups, these fragment ions cannot be used to distinguish between the two structures. Indeed, the METLIN annotation scores are comparable for both structures and are insufficient to distinguish between the isomers (Figure S2b). By using the experimental CCS value of 174.3 $Å^2$ as an additional molecular descriptor, we unambiguously identified this molecule as AMP with a reference CCS value of 174.1 $Å^2$ [37]. Meanwhile, the CCS value of 169.4 $Å^2$ reported for dGMP is substantially lower than the experimentally measured CCS, which allows us to rule out this assignment. Similarly, a feature at *m/z* 146.0461 could be assigned as the $[M-H]^-$ ion of acetylserine, methylapartate, or L-glutamate. Upon matching with MS/MS libraries, the highest score is obtained for L-glutamate as shown in Figure S3. The experimental CCS value of 125.3 $Å^2$ allows us to confirm this annotation.

Finally, we also used CCS values to identify fragments of chemically labile molecules. For example, we found multiple features for *m/z* 111.0201 at DT 16.54, 17.36 and 18.01 ms as shown in Figure S4. Based on the accurate *m/z*, the peak at *m/z* 111.0201 could be attributed to uracil. However, the CCS values of 135.9 $Å^2$, 142.6 $Å^2$ and 147.8 $Å^2$ obtained for the three DT features respectively, largely deviate from the reference value of 113.5 $Å^2$ reported for uracil [37]. These results suggest that ions at *m/z* 111.0201 observed in this experiment are likely fragments of larger molecules such as uridine mono- and di-phosphate, among others. In-source fragmentation is a common process affecting the results of untargeted metabolomics experiments [56]. Our results indicate that MSI data likely contain a fraction of features produced through in-source fragmentation, which may be mistaken for endogenous molecules. IM separation is particularly advantageous for the identification of such experimental artifacts which is important for quantitative accuracy.

Figure 3 displays drift time-separated ion images obtained for molecules in mouse uterine tissues in positive mode (top row) and negative mode (bottom row). Different regions of of the uterine tissue sections including myometrium (Myo) which is composed of longitudinal (L) and circular (C) muscle layers, stroma (S), luminal epithelium (LE), and glandular epithelium (GE) are indicated in the optical image. Representative ion images of endogenous molecules highlight different patterns of region-specific molecular distributions observed in uterine tissue sections. For example, ion images corresponding to monoglyceride (MG) 18:1, sphingomyelin (SM) d34:1, phosphatidylglycerol (PG) 34:1 and FA 22:6 display a substantial enhancement in the LE and GE cells. Meanwhile, a complementary distribution is observed for lysoPC 18:0, phosphatidylserine (PS) 40:6 and PC 32:0, which are depleted in both LE and GE. Most metabolites display a less delineated distribution. For example, inosine monophosphate (IMP) is suppressed in both the LE and adjacent stroma cells but isabundant outside of this region. In contrast, AMP is evenly distributed across the stroma. Finally, some molecules such as taurine are evenly distributed across the entire tissue. Identification of these and other biologically lipid molecules in situ is important for understanding uterine biology during pregnancy.

The spatial resolution of ~25 μm was estimated for dritft-time separated ion images based on the 20/80 rule as shown in Figure S5 [50,57]. In comparison, spatial resolution of 10 μm has been previously obtained using a similar high-resolution nano-DESI probe [50,58]. We propose that the spatial resolution in this experiment was limited by the acquisition rate of the mass spectrometer rather than the size of the liquid bridge. In particular, we used the acquisition rate of 1 Hz, which provides good-quality IM-MS data. Based on the scan rate of 20 μm/s used in this experiment, the pixel size along the scan direction is 20 μm at 1 Hz acquisition rate. The spatial resolution can be improved using faster acquisition rates at the expense of sensitivity. For example, as shown in Figure S6, the S/N ratio at 782.5655 increases from 915 at 7 Hz to 1699 at 1 Hz due to an increase in the number of mass spectra averaged per pixel. In summary, these results demonstrate the successful implementation of the high-resolution nano-DESI MSI on the IM-QTOF instruments, which provides high-quality ion images of drift time-separated ions. Furthermore, the portable platform constructed in this study, enables the implementation of nano-DESI MSI on any commercial mass spectrometer. Indeed, we were able to use this platform in combination with an ion trap mass spectrometer in our laboratory.

Separation of isomeric species

Isomeric separation is a unique capability that greatly enhances chemical coverage of MSI experiments. However, the complexity of lipid isomeric structures makes their drift time separation challenging. It has been demonstrated that the resolving power of greater than 250 is often necessary for the isomeric

separation of lipids using IM [59]. However, a majority of DTIMS instruments, such as the one used in our experiments, have the IM resolving power of ~60. We identified many unresolved features in the IM-MSI data based on the widths of the peaks, suggesting the presence of multiple isomeric components. Because our current data analysis tools can only be used to obtain ion images of well-separated features, we performed the analysis of selected unresolved peaks using manual data extraction. Specifically, we used peak fitting to extract the abundance of each isomeric component and generate isomer-specific ion images.

Figure 4 illustrates this approach. The experimental arrival time distribution of *m/z* 343.2272 identified as an oxidized FA is shown as a dotted line in Figure 4a. We observe that the peak shape is not symmetrical and shows a shoulder at longer drift times. Without peak deconvolution, our imaging workflow would only select the peak centered at DT 24.91 ms as highlighted by the yellow bar. The optical image is shown in Figure 4b whereas the corresponding ion image generated from the region highlighted with a yellow bar is shown in Figure 4c. It can be observed that this molecule is enhanced in the GE and LE region of the tissue. Using peak fitting, we identified the presence of at least two isomeric components. The peak of the first isomeric component (blue line) is centered at DT 24.91 ms and the second isomeric component (pink line) is centered at DT 25.52 ms. The spatial distributions of the two isomeric components were obtained by selecting regions of the IM peak where the contribution from the other isomer is small as illustrated in Figures 4d and 4e. Fractional distribution images (FDI) were obtained by plotting the abundance ratio of the signal obtained for isomer 1 over the total signal of both isomers (Figure 4f). Although both isomers of *m/z* 343.2272 are localized to the same regions of the tissue, the FDI image shows that their relative abundance varies across the tissue. Specifically, isomer 1 is more abundant in myometrium and stroma and suppressed in the LE region in comparison with isomer 2. Similar analysis was performed for other oxidized FAs at *m/z* 345.2422 and *m/z* 347.2585 as shown in Figures S7-S9, and their FDI distributions are similar to that of *m/z* 343.2272.

The molecule at *m/z* 343.2272 was putatively identified based on the accurate *m/z* measurement as hydroxydocosahexaenoic acid (HDoHE), which is the oxidized form of FA 22:6. It is reasonable to assume that the two isomeric components observed in Figure 4a, result from the addition of the OH group to different double bond locations, which generates several isomeric oxidized species observed in the broad drift time distribution. Although the ion signal of these molecules is insufficient to collect MS/MS spectra, their CCS values provide insights into their structures. In particular, the peak centered at DT 24.91 ms has a CCS value of 189.6 $Å^2$, whereas the peak centered at DT 25.52 ms has a CCS value of 194.2 $Å^2$. Upon matching to open CCS databases, these molecules are assigned as 14- HDoHE and 17-HDoHE, respectively [37,38]. Lipid oxidation may result from the oxidative stress during pregnancy [9,60]. This inflammatory response increases the concentration of reactive oxygen species, which react with free FAs and cause

oxidation. These species are typically present at low concentrations and are difficult to identify using MS/MS. Our results demonstrate the power of IM separation for distinguishing variations in the localization of isomeric species in biological tissues, which cannot be achieved based on the accurate *m/z* measurement alone. This capability along with improved identification of molecules based on their CCS values obtained using DTIMS is critical to obtaining accurate imaging and identification of molecules in biological samples in the same experiment. Despite these advantages, the resolving power of DTIMS may be insufficient to fully separate isomeric lipids. This limitation may be partially addressed using advanced data processing approaches. We are currently developing tools that will allow us to extract features from unresolved peaks to further expand the depth of chemical information, which may be obtained using IM-MSI. The resolving power of DTIMS may be further improved using higher-pressure instruments [61,62].

IM-MSI eliminates interferences from isobaric peaks

IM separation in nano-DESI MSI experiments is also a powerful tool for eliminating different types of interferences from imaging data. For example, the monoisotopic peak of glutathione (GSH) contains a contribution from one of the isotopes of the doubly charged oxidized glutathione (GSSG), which may alter the spatial distribution of this important molecule observed in MSI. GSH is a powerful antioxidant tripeptide produced in cells which is comprised of glutamic acid, cysteine, and glycine whereas its oxidized form, GSSG, is comprised of two molecules of GSH linked by a disulfide bridge. IM-MSI experiments reveal that the monoisotopic peak of $[GSH-H]^-$ at *m/z* 306.0758 overlaps with the M+2 isotope of $[GSSG-2H]^{2-}$ at *m/z* 306.0748. Separation of these two peaks in the *m/z* domain requires a mass resolving power of >300,000 which is challenging even for high mass resolution instruments such as Orbitraps. In contrast, these peaks are readily separated in the drift time domain as shown in Figure 5. Specifically, Figure 5a shows the 2D IM-MS map for the *m/z* range of 304.5-307.5, in which the isotopic distributions for GSH and GSSG are indicated by an orange and purple line, respectively. The two isobaric components at *m/z* 306 are readily separated in the IM dimension with one peak observed at DT of 17.85 ms and another one at 21.29 ms. Ion images generated for these two components depict distinct spatial localization as shown in Figures 5b and 5c. The molecule at DT 17.85 ms is enhanced in the longitudinal muscle layer and stroma whereas the molecule at 21.29 ms is enhanced in the circular muscle layer and stroma. Although the distribution of GSSG can be readily obtained by selecting the monoisotopic peak at *m/z* 305.0695, the distribution of GSH at *m/z* 306.0754 is altered by the contribution of the M+2 isotope of GSSG, which cannot be accounted for without IM separation. An overlay of the two peak components is depicted in Figure 5d where it can be clearly observed how each of them contributes to the ion image. IM separation is critical to eliminating this type of interference, which may affect biological insights derived from MSI data. For example, the ratio of GSH to GSSG is commonly used to evaluate the oxidative stress within cells with

the lower ratio associated with an onset of neurodegenerative diseases [63,64]. Therefore, accurate measurement of the GSH to GSSG ratio across the tissue may be only obtained using IM-MSI experiments.

Separation of isobaric peaks using IM-MSI is not limited to the overlapping isotopic distributions. Previously, the isobaric differentiation in IM-MSI was used to distinguish between isobaric peptides fragments corresponding to tubulin and ubiquitin [65]. The reconstructed ion images of these proteins showed remarkably different distributions in rat brain tissue sections. In our positive mode data, we observed that some PC and PE species were not separated in the *m/z* dimension using the extended dynamic range (2 GHz) mode selected in this study. For example, in Figure S10 we show two neighboring ions at *m/z* 818.5637 and 818.6019, which were identified as sodiated PE(40:4) and PC(P-38:3), respectively. Separation of these species with a mass difference of 0.0364 Da corresponding to the difference between CH_4 and O, requires a mass resolving power of 33,000 at *m/z* 818.6019, which is higher than the mass resolving power of the IM-QTOF in the extended dynamic range mode ($m/\Delta m$ = 23,500 at *m/z* 782.5653). Although the two isobaric peaks are not well-separated in the *m/z* dimension, they are readily separated in the IM mode. This indicates that IM separation relaxes the constraints imposed on the mass resolving power of a mass spectrometer making it possible to perform MSI experiments using less expensive instrumentation and thereby making it more accessible to the scientific community.

Background solvent peaks are also eliminated as shown in Figure S11 which illustrates the separation of LPC(18:2) as a $[M+Na]^+$ ion at *m/z* 542.3208 from an isobaric solvent peak at *m/z* 542.2983. It can be clearly observed that the spatial distribution of LPC(18:2) is completely masked by the background peak in the MS mode. Meanwhile, a distinct pattern showing that this molecule is depleted in both LE and GE is observed in the IM-MS mode. This capability has been previously used in MALDI-IMS-MSI experiments to obtain high-quality ion images of endogenous lipids in breast tumor tissue by reducing the interference from matrix ions [66]. Collectively, these results demonstrate the power of IM-MSI for obtaining ion images free of isobaric interferences, which present a challenge to the accurate measurement of concentration gradients and data interpretation.

CONCLUSIONS

In this work, we expanded the analytical capabilities of nano-DESI MSI by successfully coupling it with IM separation, which opens up new opportunities for the spatially-resolved analysis of complex biological samples. An important advantage of our newly developed nano-DESI platform is that it is portable and can be interfaced with any commercial mass spectrometer. Coupling of IM separation with nano-DESI MSI eliminates interferences and enables accurate measurements of concentration gradients of both isomeric and isobaric endogenous molecules extracted from the sample thereby increasing the molecular specificity

of MSI. Meanwhile, the CCS values obtained from drift time measurements facilitate the identification of molecules observed in IM-MSI experiments. Future studies will focus on improving the sensitivity of the IM-MSI experiments to enable the detection of low-abundance species. This may be achieved using multiplexing strategies, which improve the sensitivity of IM experiments at no expense to the throughput. Our first proof-of-concept experiments indicate that the new nano-DESI-IM-MSI platform improves the depth of structural information and accuracy of MSI experiments, which will have a significant impact on biological and clinical research.

ACKNOWLEDGMENTS

This research is supported by the grants from the National Science Foundation (NSF-1808136 and NSF-2108729, JL) and National Institute of Health (R01HD068524-4 & R01HD103475-25 SKD). DMS acknowledges support from the National Science Foundation Graduate Research Fellowship under Grant No. (DGE-1333468). Any opinions, findings, and conclusions or recommendations expressed in this material are those of the authors and do not necessarily reflect the views of the NSF or NIH. We would like to thank to Pei Su, Dr. Ruwan T. Kurulugama, and Dr. John Fjeldsted for their technical assistance with the QTOF instrument and data analysis workflow used in this study.

ASSOCIATED CONTENT

Supporting Information. The Supporting Information is available free of charge at xxxx

AUTHOR STATEMENT

DU and JL designed the study and co-wrote the manuscript. DU performed the imaging experiments and processed the data. RY and MY also contributed in the data collection. XS, YL and SKD provided the uterine tissue sections and XS and SKD were involved in the interpretation of the results. D.M.S. developed approaches for processing and visualization of the imaging data.

DECLARATION OF COMPETING INTEREST

The authors declare no competing interests.

REFERENCES

[1] M. Stoeckli, P. Chaurand, D.E. Hallahan, R.M. Caprioli, Imaging mass spectrometry: a new technology for the analysis of protein expression in mammalian tissues, Nat. Med. 7 (2001) 493–496. doi:10.1038/86573.

[2] C. Wu, A.L. Dill, L.S. Eberlin, R.G. Cooks, D.R. Ifa, Mass spectrometry imaging under ambient conditions, Mass Spectrom. Rev. 32 (2013) 218–243. doi:10.1002/mas.21360.

[3] A. Nilsson, R.J.A. Goodwin, M. Shariatgorji, T. Vallianatou, P.J.H. Webborn, P.E. Andrén, Mass spectrometry imaging in drug development, Anal. Chem. 87 (2015) 1437–1455. doi:10.1021/ac504734s.

[4] E.J. Lanni, S.S. Rubakhin, J. V. Sweedler, Mass spectrometry imaging and profiling of single cells, J. Proteomics. 75 (2012) 5036–5051. doi:10.1016/j.jprot.2012.03.017.

[5] A.R. Buchberger, K. DeLaney, J. Johnson, L. Li, Mass spectrometry imaging: a review of emerging advancements and future insights, Anal. Chem. 90 (2018) 240–265. doi:10.1021/acs.analchem.7b04733.

[6] L.A. McDonnell, R.M.A. Heeren, Imaging mass spectrometry, Mass Spectrom. Rev. 26 (2007) 606–643. doi:10.1002/mas.20124.

[7] Y. Tsubata, M. Hayashi, R. Tanino, H. Aikawa, M. Ohuchi, K. Tamura, Y. Fujiwara, T. Isobe, A. Hamada, Evaluation of the heterogeneous tissue distribution of erlotinib in lung cancer using matrix-assisted laser desorption ionization mass spectrometry imaging, Sci. Rep. 7 (2017) 12622. doi:10.1038/s41598-017-13025-8.

[8] A.K. Jarmusch, V. Pirro, Z. Baird, E.M. Hattab, A.A. Cohen-Gadol, R.G. Cooks, Lipid and metabolite profiles of human brain tumors by desorption electrospray ionization-MS, Proc. Natl. Acad. Sci. U. S. A. 113 (2016) 1486–1491. doi:10.1073/pnas.1523306113.

[9] I. Lanekoff, J. Cha, J.E. Kyle, S.K. Dey, J. Laskin, K.E. Burnum-Johnson, Trp53 deficient mice predisposed to preterm birth display region-specific lipid alterations at the embryo implantation site, Sci. Rep. 6 (2016) 33023. doi:10.1038/srep33023.

[10] V. Garikapati, S. Karnati, D.R. Bhandari, E. Baumgart-Vogt, B. Spengler, High-resolution atmospheric-pressure MALDI mass spectrometry imaging workflow for lipidomic analysis of late fetal mouse lungs, Sci. Rep. 9 (2019) 3192. doi:10.1038/s41598-019-39452-3.

[11] S.E. Dautel, J.E. Kyle, G. Clair, R.L. Sontag, K.K. Weitz, A.K. Shukla, S.N. Nguyen, Y.M. Kim, E.M. Zink, T. Luders, C.W. Frevert, S.A. Gharib, J. Laskin, J.P. Carson, T.O. Metz, R.A. Corley, C. Ansong, Lipidomics reveals dramatic lipid compositional changes in the maturing postnatal lung, Sci. Rep. 7 (2017) 40555. doi:10.1038/srep40555.

[12] A.L. Bruinen, C. Van Oevelen, G.B. Eijkel, M. Van Heerden, F. Cuyckens, R.M.A. Heeren, Mass Spectrometry Imaging of Drug Related Crystal-Like Structures in Formalin-Fixed Frozen and Paraffin-Embedded Rabbit Kidney Tissue Sections, J. Am. Soc. Mass Spectrom. 27 (2016) 117–123. doi:10.1007/s13361-015-1254-3.

[13] T. Rao, Y. Shao, N. Hamada, Y. Li, H. Ye, D. Kang, B. Shen, X. Li, X. Yin, Z. Zhu, H. Li, L. Xie, G. Wang, Y. Liang, Pharmacokinetic study based on a matrix-assisted laser desorption/ionization quadrupole ion trap time-of-flight imaging mass microscope combined with a novel relative exposure approach: A case of octreotide in mouse target tissues, Anal. Chim. Acta. 952 (2017) 71–80. doi:10.1016/j.aca.2016.11.056.

[14] B.R. Hamilton, D.L. Marshall, N.R. Casewell, R.A. Harrison, S.J. Blanksby, E.A.B. Undheim, Mapping Enzyme Activity on Tissue by Functional Mass Spectrometry Imaging, Angew. Chemie - Int. Ed. 59 (2020) 3855–3858. doi:10.1002/anie.201911390.

[15] L.S. Eberlin, C.R. Ferreira, A.L. Dill, D.R. Ifa, R.G. Cooks, Desorption electrospray ionization

mass spectrometry for lipid characterization and biological tissue imaging, Biochim. Biophys. Acta - Mol. Cell Biol. Lipids. 1811 (2011) 946–960. doi:10.1016/j.bbalip.2011.05.006.

[16] B. Spengler, Mass spectrometry imaging of biomolecular information, Anal. Chem. 87 (2015) 64–82. doi:10.1021/ac504543v.

[17] D. Gode, D.A. Volmer, Lipid imaging by mass spectrometry-a review, Analyst. 138 (2013) 1289–1315. doi:10.1039/c2an36337b.

[18] D.S. Cornett, M.L. Reyzer, P. Chaurand, R.M. Caprioli, MALDI imaging mass spectrometry: molecular snapshots of biochemical systems, Nat. Methods. 4 (2007) 828–833. doi:10.1038/nmeth1094.

[19] P.J. Roach, J. Laskin, A. Laskin, Nanospray desorption electrospray ionization: An ambient method for liquid-extraction surface sampling in mass spectrometry, Analyst. 135 (2010) 2233–2236. doi:10.1039/c0an00312c.

[20] J. Laskin, B.S. Heath, P.J. Roach, L. Cazares, O.J. Semmes, Tissue imaging using nanospray desorption electrospray ionization mass spectrometry, Anal. Chem. 84 (2012) 141–148. doi:10.1021/ac2021322.

[21] H.-M. Bergman, E. Lundin, M. Andersson, I. Lanekoff, Quantitative mass spectrometry imaging of small-molecule neurotransmitters in rat brain tissue sections using nanospray desorption electrospray ionization, Analyst. 141 (2016) 3686–3695. doi:10.1039/C5AN02620B.

[22] I. Lanekoff, M. Thomas, J.P. Carson, J.N. Smith, C. Timchalk, J. Laskin, Imaging Nicotine in Rat Brain Tissue by Use of Nanospray Desorption Electrospray Ionization Mass Spectrometry, Anal Chem. 85 (2013) 882–889. doi:Doi 10.1021/Ac302308p.

[23] I. Lanekoff, S.L. Stevens, M.P. Stenzel-Poore, J. Laskin, Matrix effects in biological mass spectrometry imaging: identification and compensation, Analyst. 139 (2014) 3528–3532. doi:10.1039/c4an00504j.

[24] K.E. Burnum, D.S. Cornett, S.M. Puolitaival, S.B. Milne, D.S. Myers, S. Tranguch, H.A. Brown, S.K. Dey, R.M. Caprioli, Spatial and temporal alterations of phospholipids determined by mass spectrometry during mouse embryo implantation, J. Lipid Res. 50 (2009) 2290–2298. doi:10.1194/jlr.M900100-JLR200.

[25] I. Lanekoff, K. Burnum-Johnson, M. Thomas, J. Short, J.P. Carson, J. Cha, S.K. Dey, P. Yang, M.C. Prieto Conaway, J. Laskin, High-speed tandem mass spectrometric in situ imaging by nanospray desorption electrospray ionization mass spectrometry, Anal. Chem. 85 (2013) 9596–9603. doi:10.1021/ac401760s.

[26] D. Unsihuay, P. Su, H. Hu, J. Qiu, S. Kuang, Y. Li, X. Sun, S.K. Dey, J. Laskin, Inside Cover: Imaging and Analysis of Isomeric Unsaturated Lipids through Online Photochemical Derivatization of Carbon–Carbon Double Bonds (Angew. Chem. Int. Ed. 14/2021), Angew. Chemie Int. Ed. 60 (2021) 7450–7450. doi:10.1002/anie.202102052.

[27] A. Bednařík, S. Bölsker, J. Soltwisch, K. Dreisewerd, An On-Tissue Paternò–Büchi Reaction for Localization of Carbon–Carbon Double Bonds in Phospholipids and Glycolipids by Matrix-Assisted Laser-Desorption–Ionization Mass-Spectrometry Imaging, Angew. Chemie - Int. Ed. 57 (2018) 12092–12096. doi:10.1002/anie.201806635.

[28] A. Bednařík, J. Preisler, D. Bezdeková, M. Machálková, M. Hendrych, J. Navrátilová, L. Knopfová, E. Moskovets, J. Soltwisch, K. Dreisewerd, Ozonization of Tissue Sections for MALDI

MS Imaging of Carbon–Carbon Double Bond Positional Isomers of Phospholipids, Anal. Chem. 92 (2020) 6245–6250. doi:10.1021/acs.analchem.0c00641.

[29] G. Paglia, G. Astarita, Metabolomics and lipidomics using traveling-wave ion mobility mass spectrometry, Nat. Protoc. 12 (2017) 797–813. doi:10.1038/nprot.2017.013.

[30] J.N. Dodds, E.S. Baker, Ion Mobility Spectrometry: Fundamental Concepts, Instrumentation, Applications, and the Road Ahead, J. Am. Soc. Mass Spectrom. 30 (2019) 2185–2195. doi:10.1007/s13361-019-02288-2.

[31] A. Kiss, R.M.A. Heeren, Size, weight and position: ion mobility spectrometry and imaging MS combined, Anal. Bioanal. Chem. 399 (2011) 2623–2634. doi:10.1007/s00216-010-4644-1.

[32] M. Sans, C.L. Feider, L.S. Eberlin, Advances in mass spectrometry imaging coupled to ion mobility spectrometry for enhanced imaging of biological tissues, Curr. Opin. Chem. Biol. 42 (2018) 138–146. doi:10.1016/j.cbpa.2017.12.005.

[33] J.C. May, C.R. Goodwin, N.M. Lareau, K.L. Leaptrot, C.B. Morris, R.T. Kurulugama, A. Mordehai, C. Klein, W. Barry, E. Darland, G. Overney, K. Imatani, G.C. Stafford, J.C. Fjeldsted, J.A. McLean, Conformational ordering of biomolecules in the gas phase: Nitrogen collision cross sections measured on a prototype high resolution drift tube ion mobility-mass spectrometer, Anal. Chem. 86 (2014) 2107–2116. doi:10.1021/ac4038448.

[34] M.T. Bowers, Ion mobility spectrometry: A personal view of its development at UCSB, Int. J. Mass Spectrom. 370 (2014) 75–95. doi:10.1016/j.ijms.2014.06.016.

[35] B.C. Bohrer, S.I. Merenbloom, S.L. Koeniger, A.E. Hilderbrand, D.E. Clemmer, Biomolecule Analysis by Ion Mobility Spectrometry, Annu. Rev. Anal. Chem. 1 (2008) 293–327. doi:10.1146/annurev.anchem.1.031207.113001.

[36] S.M. Stow, T.J. Causon, X. Zheng, R.T. Kurulugama, T. Mairinger, J.C. May, E.E. Rennie, E.S. Baker, R.D. Smith, J.A. McLean, S. Hann, J.C. Fjeldsted, An Interlaboratory Evaluation of Drift Tube Ion Mobility-Mass Spectrometry Collision Cross Section Measurements, Anal. Chem. 89 (2017) 9048–9055. doi:10.1021/acs.analchem.7b01729.

[37] J.A. Picache, B.S. Rose, A. Balinski, K.L. Leaptrot, S.D. Sherrod, J.C. May, J.A. McLean, Collision cross section compendium to annotate and predict multi-omic compound identities, Chem. Sci. 10 (2019) 983–993. doi:10.1039/c8sc04396e.

[38] X. Zheng, N.A. Aly, Y. Zhou, K.T. Dupuis, A. Bilbao, V.L. Paurus, D.J. Orton, R. Wilson, S.H. Payne, R.D. Smith, E.S. Baker, A structural examination and collision cross section database for over 500 metabolites and xenobiotics using drift tube ion mobility spectrometry, Chem. Sci. 8 (2017) 7724–7736. doi:10.1039/c7sc03464d.

[39] P.L. Plante, É. Francovic-Fontaine, J.C. May, J.A. McLean, E.S. Baker, F. Laviolette, M. Marchand, J. Corbeil, Predicting Ion Mobility Collision Cross-Sections Using a Deep Neural Network: DeepCCS, Anal. Chem. 91 (2019) 5191–5199. doi:10.1021/acs.analchem.8b05821.

[40] S.N. Jackson, M. Ugarov, T. Egan, J.D. Post, D. Langlais, J.A. Schultz, A.S. Woods, MALDI-ion mohility-TOFMS imaging of lipids in rat brain tissue, J. Mass Spectrom. 42 (2007) 1093–1098. doi:10.1002/jms.1245.

[41] J.M. Spraggins, K. V. Djambazova, E.S. Rivera, L.G. Migas, E.K. Neumann, A. Fuetterer, J. Suetering, N. Goedecke, A. Ly, R. Van De Plas, R.M. Caprioli, High-Performance Molecular Imaging with MALDI Trapped Ion-Mobility Time-of-Flight (timsTOF) Mass Spectrometry, Anal.

Chem. 91 (2019) 14552–14560. doi:10.1021/acs.analchem.9b03612.

[42] C.L. Feider, N. Elizondo, L.S. Eberlin, Ambient ionization and FAIMS mass spectrometry for enhanced imaging of multiply charged molecular ions in biological tissues, Anal. Chem. 88 (2016) 11533–11541. doi:10.1021/acs.analchem.6b02798.

[43] R. V. Bennett, C.M. Gamage, A.S. Galhena, F.M. Fernández, Contrast-enhanced differential mobility-desorption electrospray ionization-mass spectrometry imaging of biological tissues, Anal. Chem. 86 (2014) 3756–3763. doi:10.1021/ac5007816.

[44] R.L. Griffiths, J.W. Hughes, S.E. Abbatiello, M.W. Belford, I.B. Styles, H.J. Cooper, Comprehensive LESA Mass Spectrometry Imaging of Intact Proteins by Integration of Cylindrical FAIMS, Anal. Chem. 92 (2020) 2885–2890. doi:10.1021/acs.analchem.9b05124.

[45] B. Shrestha, A. Vertes, High-throughput cell and tissue analysis with enhanced molecular coverage by laser ablation electrospray ionization mass spectrometry using ion mobility separation, Anal. Chem. 86 (2014) 4308–4315. doi:10.1021/ac500007t.

[46] M. Ekelöf, J. Dodds, S. Khodjaniyazova, K.P. Garrard, E.S. Baker, D.C. Muddiman, Coupling IR-MALDESI with Drift Tube Ion Mobility-Mass Spectrometry for High-Throughput Screening and Imaging Applications, J. Am. Soc. Mass Spectrom. 31 (2020) 642–650. doi:10.1021/jasms.9b00081.

[47] M. Sans, C.L. Feider, L.S. Eberlin, Advances in mass spectrometry imaging coupled to ion mobility spectrometry for enhanced imaging of biological tissues, Curr. Opin. Chem. Biol. 42 (2018) 138–146. doi:10.1016/j.cbpa.2017.12.005.

[48] I. Lanekoff, M. Thomas, J. Laskin, Shotgun approach for quantitative imaging of phospholipids using nanospray desorption electrospray ionization mass spectrometry, Anal. Chem. 86 (2014) 1872–1880. doi:10.1021/ac403931r.

[49] I. Lanekoff, K. Burnum-Johnson, M. Thomas, J. Cha, S.K. Dey, P. Yang, M.C. Prieto Conaway, J. Laskin, Three-dimensional imaging of lipids and metabolites in tissues by nanospray desorption electrospray ionization mass spectrometry, Anal. Bioanal. Chem. 407 (2015) 2063–2071. doi:10.1007/s00216-014-8174-0.

[50] R. Yin, K.E. Burnum-Johnson, X. Sun, S.K. Dey, J. Laskin, High spatial resolution imaging of biological tissues using nanospray desorption electrospray ionization mass spectrometry, Nat. Protoc. 14 (2019) 3445–3470. doi:10.1038/s41596-019-0237-4.

[51] S.N. Nguyen, A. V. Liyu, R.K. Chu, C.R. Anderton, J. Laskin, Constant-distance mode nanospray desorption electrospray ionization mass spectrometry imaging of biological samples with complex topography, Anal. Chem. 89 (2017) 1131–1137. doi:10.1021/acs.analchem.6b03293.

[52] D. Mesa Sanchez, S. Creger, V. Singla, R.T. Kurulugama, J.C. Fjeldsted, J. Laskin, An Ion Mobility-Mass Spectrometry Imaging Workflow, J. Am. Soc. Mass Spectrom. 0 (2020). doi:10.1021/jasms.0c00142.

[53] B. MacLean, D.M. Tomazela, N. Shulman, M. Chambers, G.L. Finney, B. Frewen, R. Kern, D.L. Tabb, D.C. Liebler, M.J. MacCoss, Skyline: An open source document editor for creating and analyzing targeted proteomics experiments, Bioinformatics. 26 (2010) 966–968. doi:10.1093/bioinformatics/btq054.

[54] K.M. Hines, J. Herron, L. Xu, Assessment of altered lipid homeostasis by HILIC-ion mobility-mass spectrometry-based lipidomics, J. Lipid Res. 58 (2017) 809–819. doi:10.1194/jlr.D074724.

[55] J.E. Kyle, N. Aly, X. Zheng, K.E. Burnum-Johnson, R.D. Smith, E.S. Baker, Evaluating lipid mediator structural complexity using ion mobility spectrometry combined with mass spectrometry, Bioanalysis. 10 (2018). doi:10.4155/bio-2017-0245.

[56] X. Domingo-Almenara, J. Rafael Montenegro-Burke, C. Guijas, E. L.-W. Majumder, H. Paul Benton, G. Siuzdak, Autonomous METLIN-Guided In-source Fragment Annotation for Untargeted Metabolomics, Anal. Chem. 91 (2019) 3246–3253. doi:10.1021/acs.analchem.8b03126.

[57] S.L. Luxembourg, T.H. Mize, L.A. McDonnell, R.M.A. Heeren, High-spatial resolution mass spectrometric imaging of peptide and protein distributions on a surface, Anal. Chem. 76 (2004) 5339–5344. doi:10.1021/ac049692q.

[58] S.N. Nguyen, R.L. Sontag, J.P. Carson, R.A. Corley, C. Ansong, J. Laskin, Towards High-Resolution Tissue Imaging Using Nanospray Desorption Electrospray Ionization Mass Spectrometry Coupled to Shear Force Microscopy, J. Am. Soc. Mass Spectrom. 29 (2018) 316–322. doi:10.1007/s13361-017-1750-8.

[59] K. V. Djambazova, D.R. Klein, L.G. Migas, E.K. Neumann, E.S. Rivera, R. Van De Plas, R.M. Caprioli, J.M. Spraggins, Resolving the Complexity of Spatial Lipidomics Using MALDI TIMS Imaging Mass Spectrometry, Anal. Chem. 92 (2020) 13290–13297. doi:10.1021/acs.analchem.0c02520.

[60] D.I. Chiarello, C. Abad, D. Rojas, F. Toledo, C.M. Vázquez, A. Mate, L. Sobrevia, R. Marín, Oxidative stress: Normal pregnancy versus preeclampsia, Biochim. Biophys. Acta - Mol. Basis Dis. 1866 (2020). doi:10.1016/j.bbadis.2018.12.005.

[61] M. Groessl, S. Graf, R. Knochenmuss, High resolution ion mobility-mass spectrometry for separation and identification of isomeric lipids, Analyst. 140 (2015) 6904–6911. doi:10.1039/c5an00838g.

[62] J. N. Dodds, J. C. May, J. A. McLean, Correlating Resolving Power, Resolution, and Collision Cross Section: Unifying Cross-Platform Assessment of Separation Efficiency in Ion Mobility Spectrometry, Anal. Chem. 89 (2017) 12176–12184. doi:10.1021/acs.analchem.7b02827.

[63] J.B. Owen, D. Allan Butterfiel, Measurement of oxidized/reduced glutathione ratio, in: Methods Mol. Biol., 2010: pp. 269–277. doi:10.1007/978-1-60761-756-3_18.

[64] O. Zitka, S. Skalickova, J. Gumulec, M. Masarik, V. Adam, J. Hubalek, L. Trnkova, J. Kruseova, T. Eckschlager, R. Kizek, Redox status expressed as GSH:GSSG ratio as a marker for oxidative stress in paediatric tumour patients, Oncol. Lett. 4 (2012) 1247–1253. doi:10.3892/ol.2012.931.

[65] J. Stauber, L. MacAleese, J. Franck, E. Claude, M. Snel, B.K. Kaletas, I.M.V.D. Wiel, M. Wisztorski, I. Fournier, R.M.A. Heeren, On-Tissue Protein Identification and Imaging by MALDI-Ion Mobility Mass Spectrometry, J. Am. Soc. Mass Spectrom. 21 (2010) 338–347. doi:10.1016/j.jasms.2009.09.016.

[66] K. Chughtai, L. Jiang, T.R. Greenwood, K. Glunde, R.M.A. Heeren, Mass spectrometry images acylcarnitines, phosphatidylcholines, and sphingomyelin in MDA-MB-231 breast tumor models, J. Lipid Res. 54 (2013) 333–344. doi:10.1194/jlr.M027961.

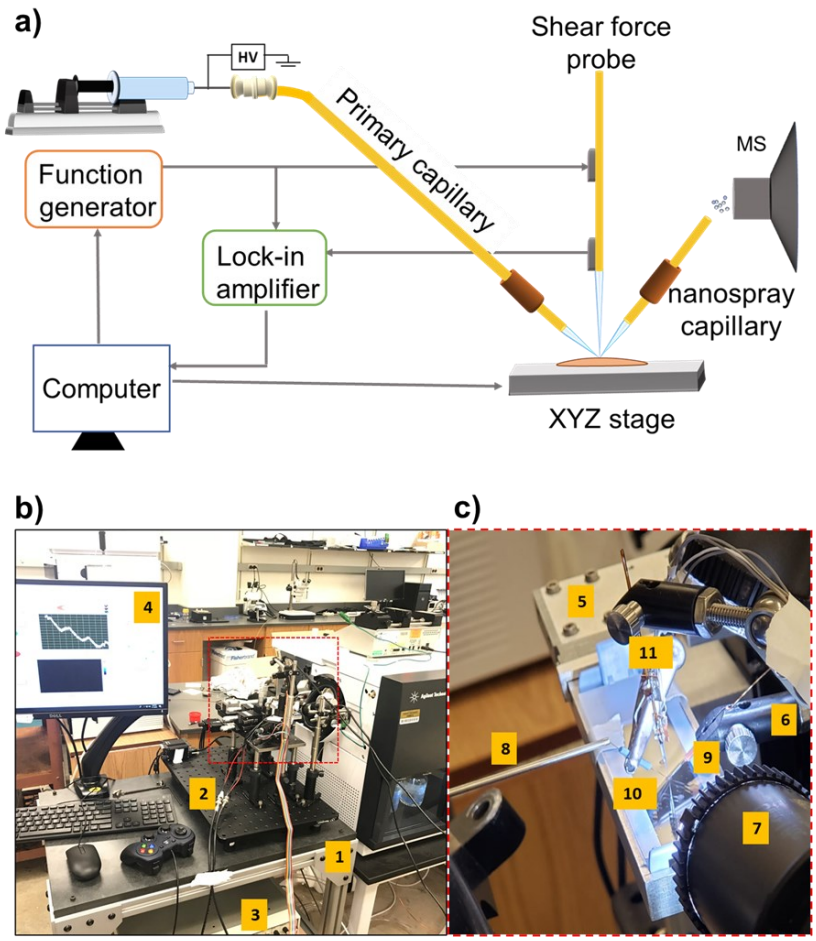

Figure 1. a) A schematic drawing of the high-resolution nano-DESI MSI source. b) A photograph of the imaging platform, showing the custom-designed cart (1); vibrationally insulated platform (2); lock-in amplifier (3), and computer that controls the XYZ stage (4). c) A zoomed-in photograph corresponding to the red dashed box in panel b. The XYZ stage (5), micro positioners (6), Dino-Lite microscope 7), capillary extension (8), primary capillary (9), nanospray capillary (10) and shear force probe (11) are also highlighted.

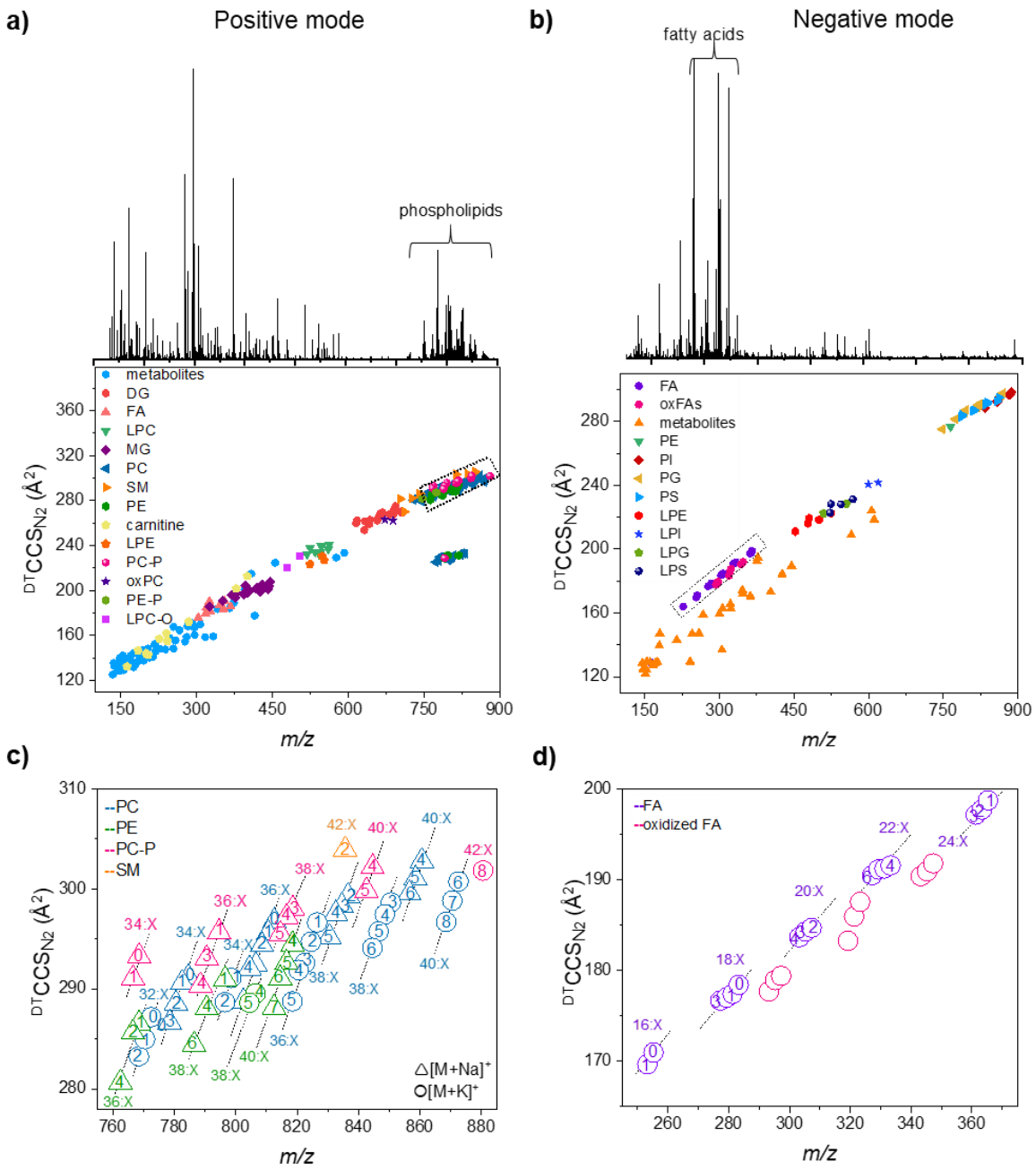

Figure 2. Averaged mass spectra and CCS vs. *m/z* plots of the species identified in the nano-DESI-IM-MSI of a mouse embryo implantation site in a) positive mode and b) negative mode. c) Phospholipids separated by drift time in the *m/z* 720-890 region highlighted with the dashed box in panel a. Triangles and circles denote $[M+Na]^+$ and $[M+K]^+$ ions, respectively, and the symbol colors indicate the lipid class of the molecule as indicated in the legend. The nomenclature used to indicate the individual species is AA:X, where AA denotes the acyl chain length and X denotes the number of double bonds. The doted lines

highlight the series of homologous species differing by the number of double bonds; the number of double bonds for each species is indicated inside the corresponding marker. d) Fatty acids and oxidized fatty acids separated by drift time in the *m/z* 250-400 region highlighted with the dashed box in panel b. Nomenclature used to indicate individual species is the same as described earlier.

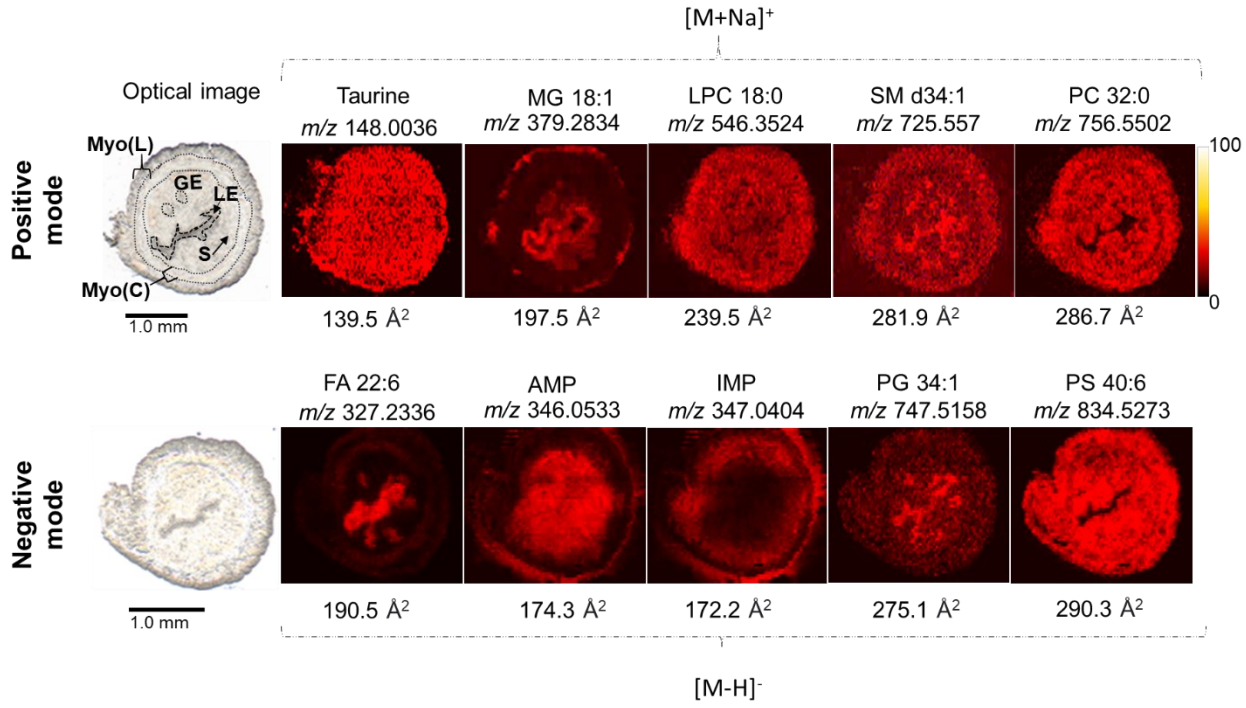

Figure 3. Optical images of the embryo implantation site tissue sections (left column) highlighting their main components including myometrium (myo) composed of longitudinal (L) and circular (C) muscle layers, stroma (S), luminal epithelium (LE) and glandular epithelium (GE) are included on the left side. Representative nano-DESI ion images of the embryo implantation site tissue sections collected using the new nano-DESI-IM-QTOF platform in positive mode (top row) and negative mode (bottom row) using 1 Hz acquisition rate. The intensity scale changes from black (low) to yellow (high).

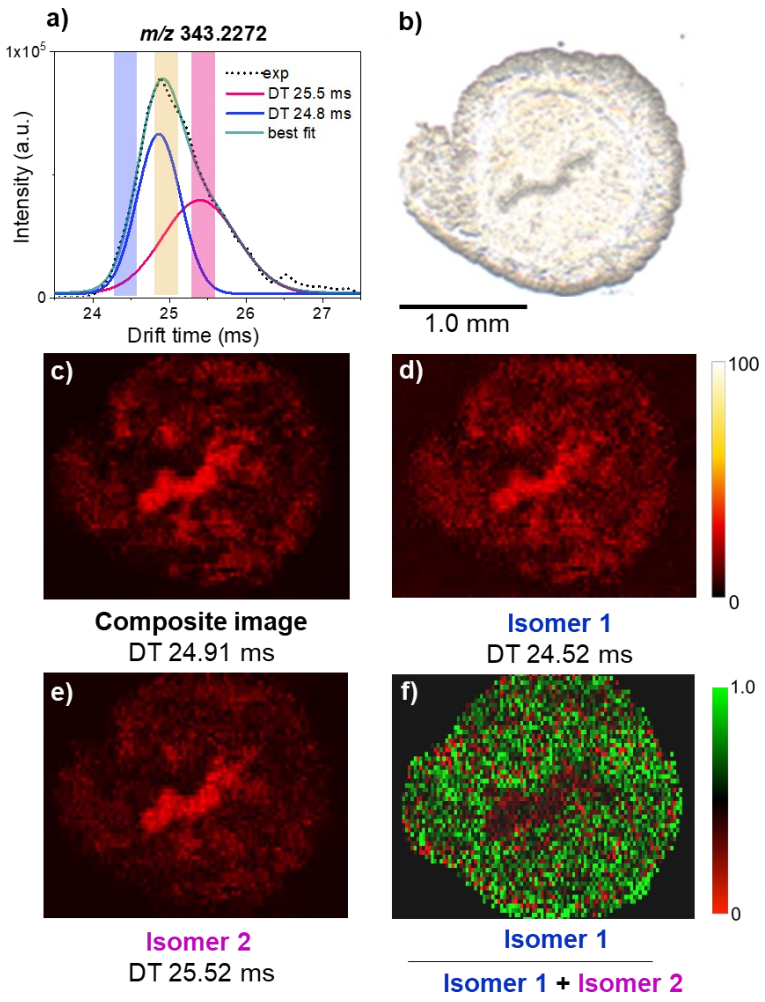

Figure 4. a) Experimental and deconvoluted arrival time distribution (ATD) of *m/z* 343.2272 The experimental ATD (dotted line) is overlaid on top of the best fit profile (solid green line). ATD profiles of isomers 1 and 2 are shown as blue and pink lines, respectively. Colored bars indicate the region selected for image generation. b) Optical image of uterine tissue section c) Composite ion image generated at DT 24.91 ms. d) Ion image of isomer 1 generated at DT 24.52 ms. e) Ion image of isomer 2 at DT 25.52 ms. d) FDI images shows that the relative abundance of isomer 1 is decreased in the LE region.

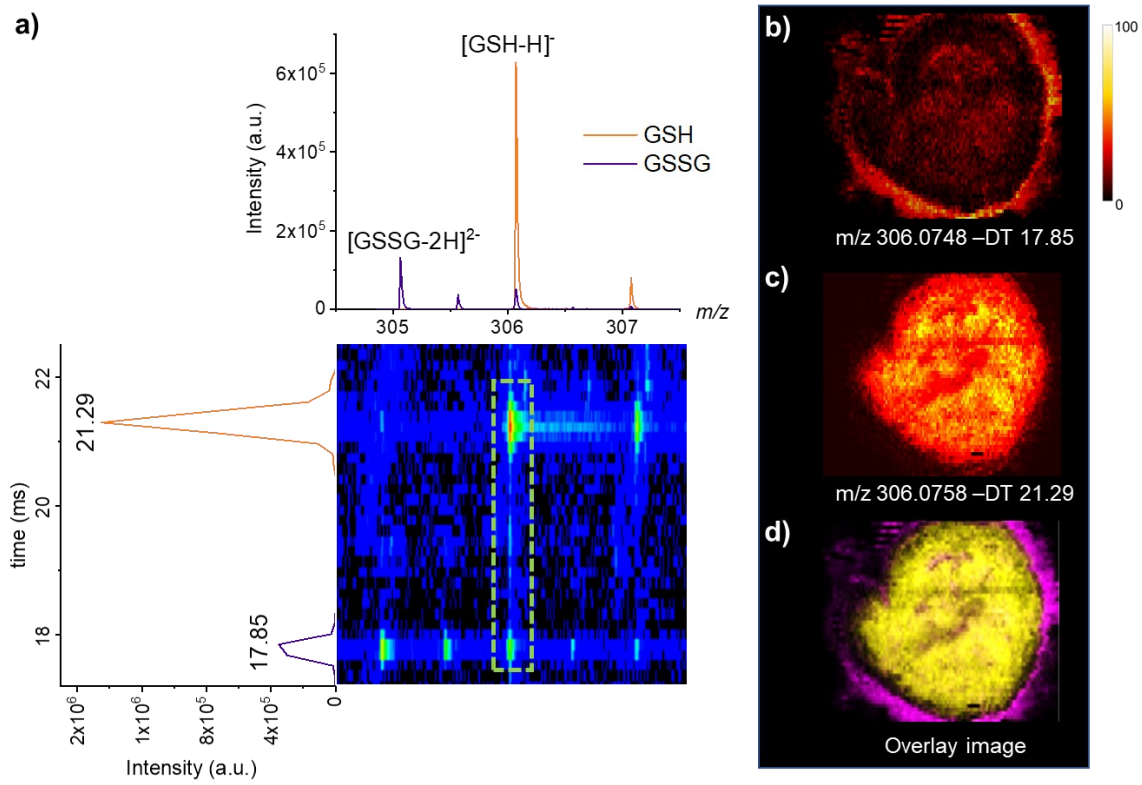

Figure 5. a) 2D-IM-MS plot of the *m/z* range of 304.5-307.5 showing the isotopic distributions of GSH (orange line) and GSSG (purple line). Ion images of closely-spaced isobaric peaks at b) *m/z* 306.0748, DT 17.85 ms and c) *m/z* 306.0758, DT 21.29 ms. d) An ion image obtained without IM separation, in which the contribution of the M+2 isotopic peak of GSSG is indicated in purple and the contribution of the monoisotopic peak of GSH in indicated in yellow.